ACS Catalysis

pubs.acs.org/acscatalysis

Research Article

Relationship between Mn Oxidation State Changes and Oxygen Reduction Activity in (La,Ca)MnO_3 as Probed by *In Situ* XAS and XES

Veronica Celorrio,* Andrew S. Leach, Haoliang Huang, Shusaku Hayama, Adam Freeman, David W. Inwood, David J. Fermin,* and Andrea E. Russell*

Cite This: *ACS Catal.* 2021, 11, 6431−6439

Read Online

ACCESS | Metrics & More | Article Recommendations | Supporting Information

ABSTRACT: *In situ* X-ray absorption and emission spectroscopies (XAS and XES) are used to provide details regarding the role of the accessibility and extent of redox activity of the Mn ions in determining the oxygen reduction activity of $LaMnO_3$ and $CaMnO_3$, with X-ray absorption near-edge structure (XANES) providing the average oxidation state, extended X-ray absorption fine structure (EXAFS) providing the local coordination environment, and XES providing the population ratios of the Mn^{2+}, Mn^{3+}, and Mn^{4+} sites as a function of the applied potential. For $LaMnO_3$, XANES and XES show that Mn^{3+} is formed, but Mn^{4+} ions are retained, which leads to the $4e^-$ reduction between 0.85 and 0.6 V. At more negative potentials, down to 0.2 V, EXAFS confirms an increase in oxygen vacancies as evidenced by changes in the Mn−O coordination distance and number, while XES shows that the Mn^{3+} to Mn^{4+} ratio increases. For $CaMnO_3$, XANES and XES show the formation of both Mn^{3+} and Mn^{2+} as the potential is made more negative, with little retention of Mn^{4+} at 0.2 V. The EXAFS for $CaMnO_3$ also indicates the formation of oxygen vacancies, but in contrast to $LaMnO_3$, this is accompanied by loss of the perovskite structure leading to structural collapse. The results presented have implications in terms of understanding of both the pseudocapacitive response of Mn oxide electrocatalysts and the processes behind degradation of the activity of the materials.

KEYWORDS: *perovskite oxides, oxygen reduction reaction, X-ray absorption/emission, $LaMnO_3$, $CaMnO_3$, manganese redox*

Downloaded via UNIV OF SOUTHAMPTON on May 27, 2021 at 12:21:39 (UTC).
See https://pubs.acs.org/sharingguidelines for options on how to legitimately share published articles.

INTRODUCTION

The increased interest in electrochemical energy-storage/conversion systems such as metal-air batteries, fuel cells, and electrolyzers arising from the interest in electrification of energy supply and distribution has motivated many studies of oxygen reduction and evolution reaction (ORR and OER) electrocatalysts.[1,2] The development of more efficient and stable materials is a critical step for the final introduction of these devices in the market. Platinum-based catalysts and IrO_2 remain as benchmark materials for the ORR and OER, respectively, in acidic and alkaline environments,[3,4] but significant efforts have also been focused on earth-abundant and low-cost materials.[5,6] A growing number of publications on the electrocatalytic properties of Co-, Ni-, and Mn-containing spinel and perovskite oxides have emerged in recent years.[7,8] The mixed valency of individual elements in the parent materials, further complicated under operating conditions, makes the identification of composition−activity relationships more difficult for such materials.[9] A deeper understanding of the contributions of each component ion to the activity is required to more fully develop such relationships and enable the design of more active/stable electrocatalysts.[9,10]

Mn-based oxides are among the most active catalysts toward the oxygen reduction reaction (ORR) in alkaline solutions. After the seminal work by Bockris and Otagawa[11] and the elegant work of Suntivich *et al.* on perovskite oxides,[12] the prevailing view is that a single electron occupancy of the e_g orbital of the metal at the B-site of the perovskite structure represents the optimum configuration for oxygen electrocatalysis. This trend implies that $LaMnO_{3+\delta}$ ($e_g \sim 1$) should be more active than $CaMnO_3$ ($e_g \sim 0$), suggesting that there is an optimal oxidation state of the active metal. However, numerous works have shown that the orbital occupancy on Mn states changes in the potential range relevant to the ORR. For example, our recent works on perovskite nanoparticles demonstrated that changes in the redox state of the B-site at Mn-based perovskites are directly linked to their activity toward the ORR.[13,14] Studies on thin films have

Received: March 3, 2021
Revised: April 27, 2021

ACS Publications

© XXXX The Authors. Published by American Chemical Society

https://doi.org/10.1021/acscatal.1c00997
ACS Catal. 2021, 11, 6431−6439

provided evidence that Mn^{3+} or a mixed valence Mn^{3+}/Mn^{4+} corresponds to the active material.[15−18] Ryabova *et al.* proposed that the potential of the Mn^{4+}/Mn^{3+} redox transition could be used as a descriptor for the ORR activity,[19] with the highest activity corresponding to the catalyst with the more positive redox potential.

Understanding the ORR mechanism at such complex materials requires direct information regarding the changes in the orbital occupancy of the Mn sites that can only be achieved using *in situ* characterization techniques. *In situ* X-ray absorption near-edge structure (XANES) studies enable identification of the oxidation states of the metal atoms, while the extended X-ray absorption fine structure (EXAFS) data enable the study of the accompanying change in oxygen coordination. For example, Gorlin *et al.*[20] and Risch *et al.*[21] concluded that manganese was reduced below Mn^{3+} and contained significant fractions of Mn^{2+} by looking at the Mn K-edge and Mn L-edge, respectively, in agreement with previous studies by Lima *et al.* at the Mn K-edge.[22] Although such X-ray absorption measurements provide element-specific information, they only enable identification of the average oxidation state of the absorbing atom owing to the energy resolution of the spectra.

The resolution of the XANES can be improved by use of a high-energy-resolution fluorescence detection (HERFD) spectrometer, which enhances the pre-edge features and detail at the edge by overcoming the core-hole lifetime broadening of the 1s hole present in conventional K-edge XANES.[23−25] The fractional contributions of the valence states to the average oxidation state can be obtained by analysis of the X-ray emission spectroscopy (XES) spectra and in particular the Kβ emission lines (3p → 1s), comprising the main K$\beta_{1,3}$ and the Kβ' satellite peaks which are sensitive to the 3d spin state of the emitting atom.[26] Traulsen *et al.* employed these methods to study the polarization-induced changes to the oxidation state of Mn for a $La_{0.5}Sr_{0.5}MnO_{3+\delta}$ solid-oxide fuel cell electrocatalyst under *operando* conditions at 500 °C, demonstrating that the average Mn oxidation state decreased from +3.4 at an open circuit to +3.2, corresponding to 34% Mn^{4+}, 49% Mn^{3+}, and 17% Mn^{2+}, at −800 mV applied potential.[27] Here, we implement electrochemical *in situ* XES and EXAFS to unravel the complex correlation between orbital occupancy of Mn sites and their electrocatalytic activities toward the ORR. For the first time, we demonstrate that electrochemical signatures associated with $LaMnO_3$ at potential close to ORR formal potential are linked to an increase in the orbital occupancy of Mn 3d sites as well as changes in the Mn−O bond distance and coordination numbers. XES enables visualization of the changes in oxidation states in terms of the population ratio of Mn^{3+} (d^4) and Mn^{4+} (d^3) states. These changes are observed at significantly more negative potential in the case of $CaMnO_3$, which is consistent with their lower activity toward the $4e^-$ ORR. Furthermore, we also observe that the structural integrity of $CaMnO_3$ is significantly more compromised upon potential cycling in comparison with $LaMnO_3$.

RESULTS

Electrocatalytic Behavior of (La,Ca)MnO_3 Oxides. Figure 1 shows the electrochemical response of $LaMnO_3$ and $CaMnO_3$ in Ar-saturated (a) and O_2-saturated (b) 0.1 M KOH solution at 0.010 V s^{-1} for electrodes with the same mass of the oxides loaded onto the glassy carbon of a rotating disk electrode. The voltammogram (Figure 1a) of $LaMnO_3$ in the Ar-saturated electrolyte features two cathodic reduction peaks, which have

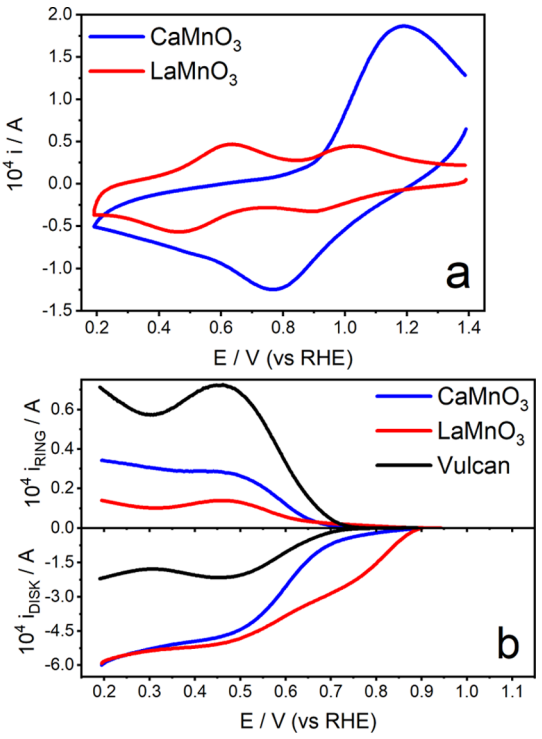

Figure 1. (a) Cyclic voltammograms of the $LaMnO_3$ and $CaMnO_3$ nanoparticles in Ar-saturated 0.1 M KOH solution at 0.010 V s^{-1}. (b) Rotating ring-disk electrode (RRDE) responses at 1600 rpm in O_2 saturated 0.1 M KOH at 0.010 V s^{-1}. The Pt ring was held at a constant potential of 1.10 V. Oxide nanoparticles were supported on a Vulcan layer (50 μg cm^{-2}) with a total oxide content of 250 μg cm^{-2}. Data for the carbon electrode were 50 μg cm^{-2}.

previously been attributed to the formation of a partially reduced state, followed by reduction to Mn^{2+}.[28−31] The corresponding voltammogram of $CaMnO_3$ is characterized by a broad reduction peak centered at 0.80 V *versus* RHE (reversible hydrogen electrode, against which all potentials in this manuscript are reported) previously ascribed to the reduction of Mn^{4+} to Mn^{2+}.[30,31] A small feature at ∼0.5 V superimposed on the main broad voltammetric peak is also observed, which may suggest the presence of Mn^{3+} sites. An increase in current and thus in the charge involved in redox processes is observed for $CaMnO_3$ compared to that for $LaMnO_3$, indicating that a larger number of Mn atoms change the oxidation state or that the change in the oxidation state for those Mn atoms that are active is larger within the potential window under study.

Figure 1b shows the disk (i_{DISK}, bottom panel) and ring (i_{RING}, top panel) currents obtained at 1600 rpm and 0.010 V s^{-1} in an O_2-saturated 0.1 M KOH solution for $LaMnO_3$ and $CaMnO_3$ in comparison with an electrode just containing Vulcan carbon. The ORR onset potential is significantly more positive than that for the Vulcan support (*ca.* 0.7 V, see black curve in Figure 1), confirming that the reaction at potentials greater than 0.7 V takes place at the oxide particles. $LaMnO_3$ presents the most positive onset potential, while $CaMnO_3$ requires a higher overpotential to initiate the reaction. Substantial peroxide detection at the ring electrode is only observed at potentials more negative than 0.7 V, indicating that the Vulcan carbon may contribute to the partial reduction of O_2 to hydrogen peroxide. However, as differences are observed between the $LaMnO_3$ and $CaMnO_3$ catalysts at potentials below 0.7 V, the $4e^-$ reduction is still taking place on the oxide. The calculated peroxide yields are

https://doi.org/10.1021/acscatal.1c00997
ACS Catal. 2021, 11, 6431−6439

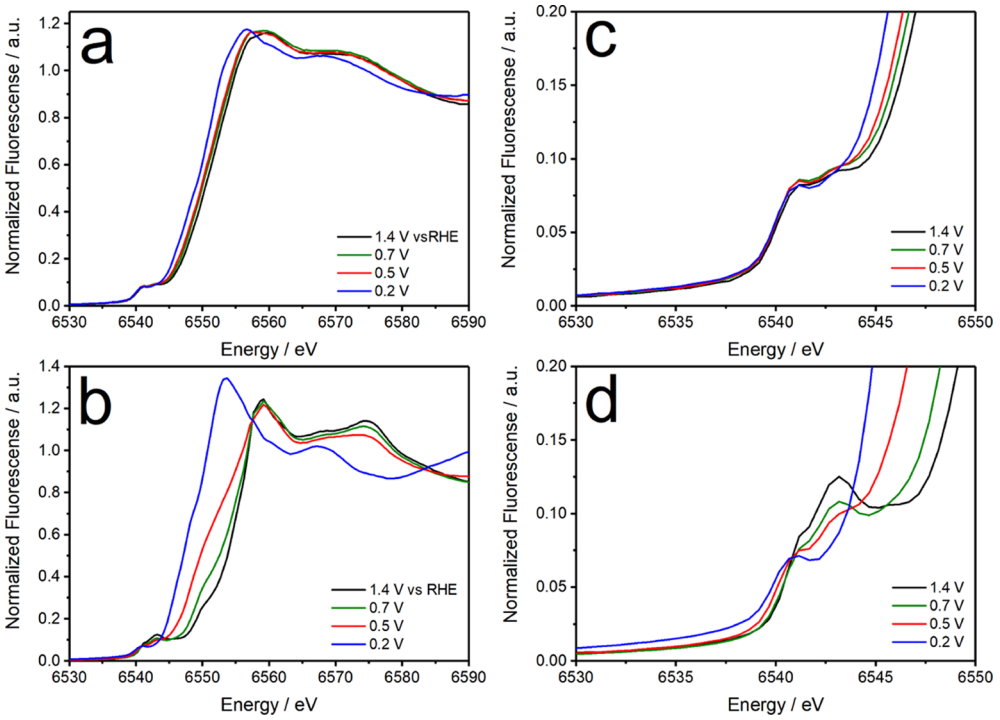

Figure 2. XANES spectra (a,b) and corresponding pre-edge regions (c,d) of the spectra at the Mn K-edge for $LaMnO_3$ (a,c) and $CaMnO_3$ (b,d) perovskite electrodes recorded at different applied potentials. Data collected in N_2-purged 0.1 M KOH.

provided as a function of the electrode potential in Figure S1. Comparing Figure 1a,b, we note that it is not until the first redox process occurs that the electrodes start generating peroxide.

***In Situ* XAS and XES Studies.** *In situ* XAS spectra were collected in standard fluorescence mode using the SAMBA beamline at SOLEIL while applying potentials relevant to the ORR, from 1.4 V to 0.2 V *versus* RHE in N_2-purged 0.1 M KOH. Figure 2 shows the XANES spectra of the $LaMnO_3$ (a) and $CaMnO_3$ (b) catalysts. For $LaMnO_3$ at 0.2 V, the edge position (determined at the half of the edge step) is shifted to lower energy by 1.2 eV relative to the spectrum at the starting potential (1.4 V), whereas for $CaMnO_3$ at 0.2 V, the edge is shifted by 6.7 eV toward lower energy compared to the starting potential. This difference is greater than the 4 eV observed between MnO_2 and Mn_2O_3 standards (Figure S2), corresponding to the Mn^{4+} and Mn^{3+} oxidation states, respectively. It is interesting to notice that for $CaMnO_3$, the position of the maximum of the white line (defined as the maximum of the rising edge) also changes at 0.2 V compared to that at 1.4 V. The average Mn oxidation state can be estimated from the edge position by reference to a calibration plot generated from the reference samples, as shown in Figure S3. The oxidation state of the $LaMnO_3$ sample determined in this manner does not show much variation with potential, +3.7 at 1.4 V going to +3.1 at 0.2 V, while that of $CaMnO_3$ shows a much more significant shift from +4.7 at 1.4 V to +2.6 at 0.2 V. However, this method is rather approximate and can yield misleading results as the edge features of Mn are also dependent on the geometry and ligand environment.[32,33] The average Mn oxidation state or number of unoccupied 3d states is more frequently probed by examination of the position of the pre-edge peak (1s → 3d) in the XANES (Figure 3c,d) following the approach by Croft *et al.*[34] The broadening and low intensity of the pre-edge features in the spectra obtained under *in situ* conditions prevents a reliable analysis of the changes in the oxidation state from these conventionally collected XANES

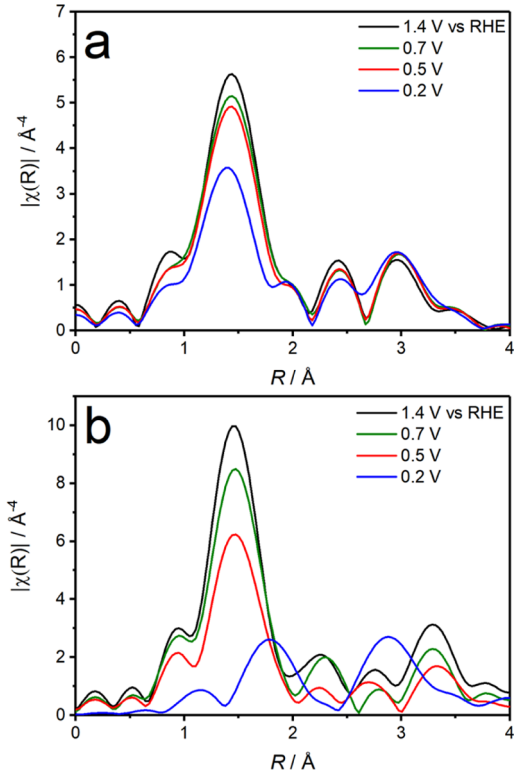

Figure 3. Fourier transforms of the k^3-weighted Mn K-edge EXAFS of $LaMnO_3$ (a) and $CaMnO_3$ (b) at different potentials. The EXAFS data and fits for the first coordination shell in both *k*- and *R*-space are shown in Figure S7 and Table S4. Data recorded in N_2-purged 0.1 M KOH at room temperature. $LaMnO_3$: $2.6 < k < 10.9$ Å^{-1}; $1.1 < R < 2.2$ Å. $CaMnO_3$: $2.5 < k < 10.1$ Å^{-1}; $1.0 < R < 2.2$ Å.

https://doi.org/10.1021/acscatal.1c00997
ACS Catal. 2021, 11, 6431−6439

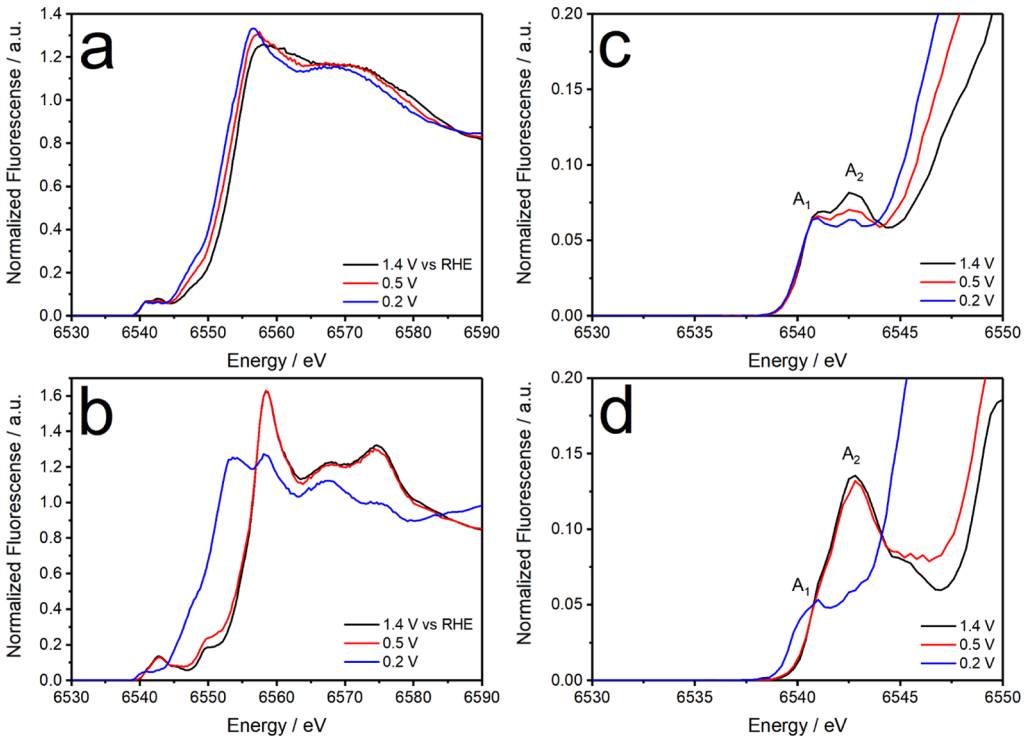

Figure 4. HERFD-XANES spectra (a,b) and corresponding pre-edge regions (c,d) obtained at the maximum of the K$\beta_{1,3}$ line of $LaMnO_3$ (a,c) and $CaMnO_3$ (b,d) as a function of the applied potential. Data recorded in N_2-purged 0.1 M KOH at room temperature.

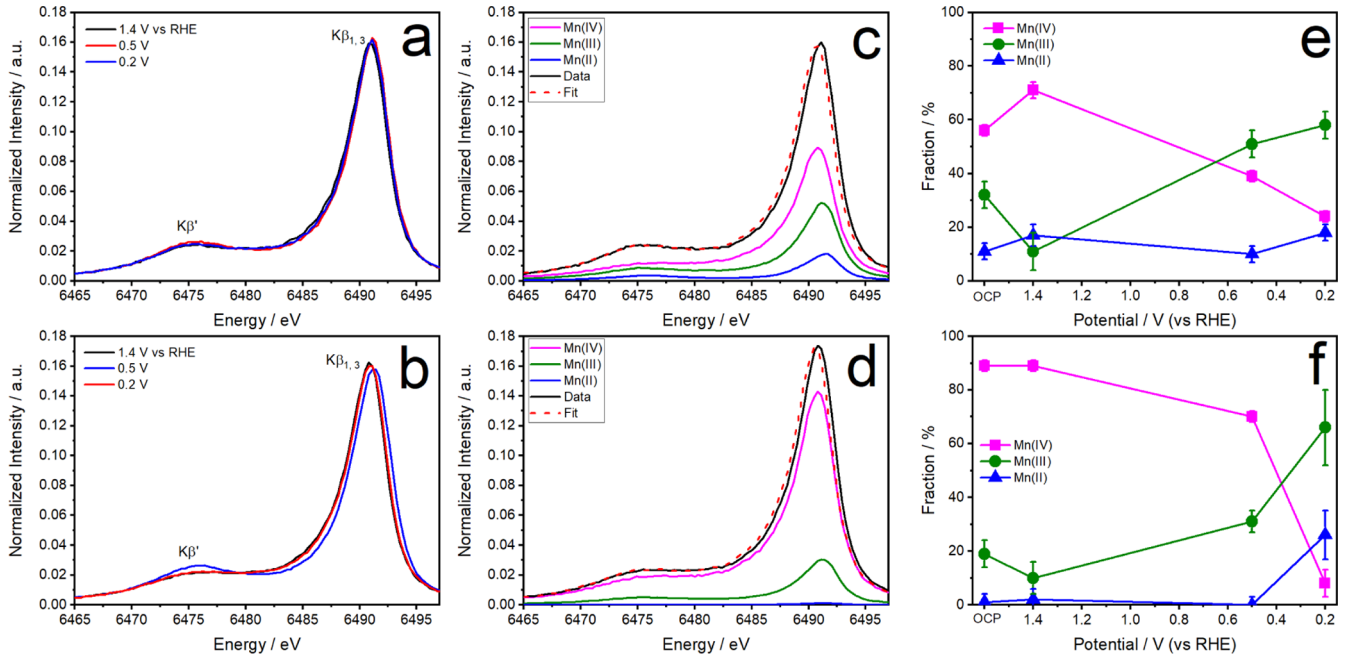

Figure 5. Normalized Mn Kβ XES spectra measured at 100 eV from the absorption edge for $LaMnO_3$ (a) and $CaMnO_3$ (b) at different applied potentials. Linear combination of the normalized Mn Kβ XES spectra for $LaMnO_3$ (c) and $CaMnO_3$ (d) for the electrodes inside the cell but without any applied potential (OCP). Percentage of the different cation species for $LaMnO_3$ (e) and $CaMnO_3$ (f) at the different potentials under study obtained by linear combination fitting of the XES data.

data. Nevertheless, very little change in the position of the pre-edge peak was observed for $LaMnO_3$ indicating only a small decrease in the average Mn oxidation state, while a more significant change is observed for the $CaMnO_3$ electrode.

Figure 3a,b shows the comparison between the Fourier transforms (FTs) of the EXAFS data at different potentials for $LaMnO_3$ and $CaMnO_3$. $LaMnO_3$ shows a decrease in amplitude for the first shell and a slight compression of the Mn−O bond at 0.2 V. In the case of $CaMnO_3$, the change with potential is much more pronounced with an expansion of the first peak to 1.8 Å and a contraction of the second shell to 2.9 Å at 0.2 V, revealing that the coordination sphere of Mn and thus the (crystal) structure change with the applied potential. Although the EXAFS of the $CaMnO_3$ dry electrode and immersed electrode at

https://doi.org/10.1021/acscatal.1c00997
ACS Catal. 2021, 11, 6431−6439

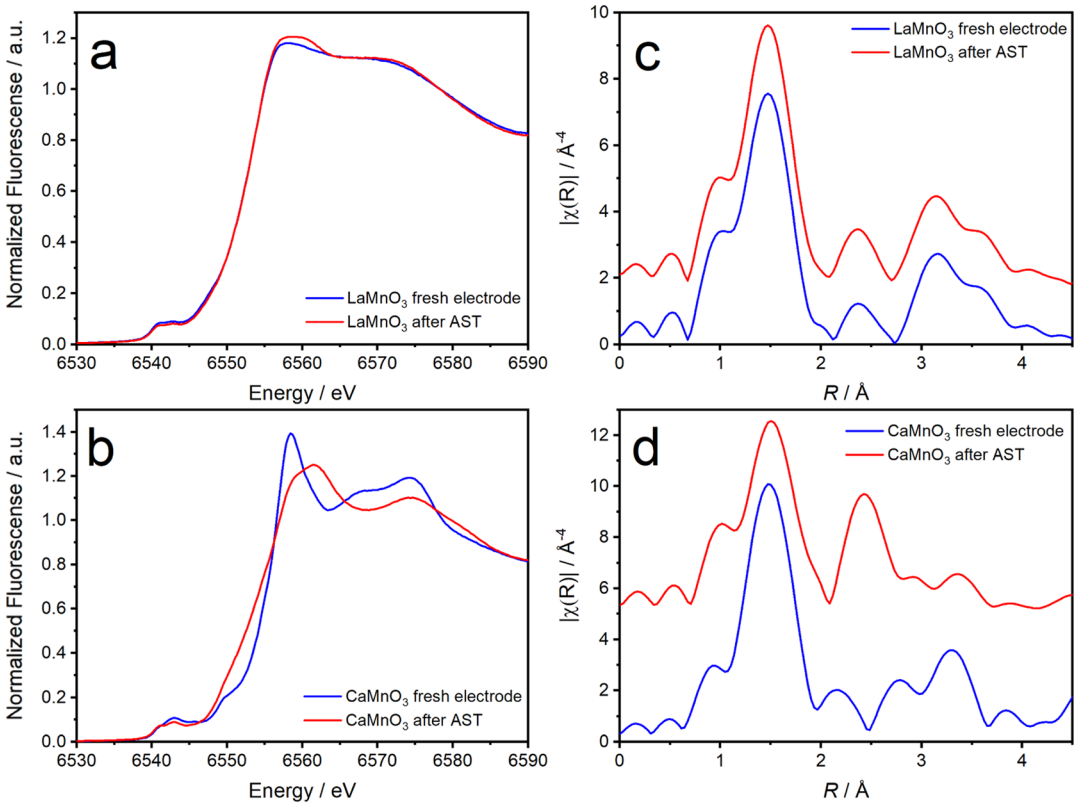

Figure 6. XANES spectra (a,b) and corresponding Fourier transforms of the k^3-weighted EXAFS (c,d) of the spectra at the Mn K-edge for $LaMnO_3$ (a,c) and $CaMnO_3$ (b,d) perovskite electrodes recorded before and after the accelerated stress test.

the starting potential of 1.4 V can still be fitted using the same structure as for the *ex situ* pellet (pellet spectra and fits provided in Figure S4 and Table S1; that for the dry electrodes in Figure S5 and Table S2; and at 1.4 V in Figure S6 and Table S3), a decrease in the amplitude of the first peak in the Fourier transforms corresponding to Mn−O coordination is observed as the potential is made more negative (Figure S7 and Table S4), which is attributed to the creation of oxygen vacancies. For $LaMnO_3$, the higher-shell structure of the perovskite is retained upon the formation of oxygen vacancies as evidenced by the peaks in the Fourier transforms at $R \geq 2$ Å. In contrast, for $CaMnO_3$, the Fourier transform and thus structure are significantly different at 0.2 V.

HERFD-XANES enhances features present in the near-edge region of the absorption spectrum.[23−25] *In situ* HERFD data and Kβ XES spectra were collected on the I20 Scanning beamline at the Diamond Light Source using a point−point Rowland circle XES spectrometer. Figure 4a,b compares the Mn K-edge HERFD-XANES as a function of potential for $LaMnO_3$ and $CaMnO_3$, respectively (data for the reference materials are shown in Figure S8). For $LaMnO_3$ (Figure 5a), decreasing the potential results in the reduction of Mn as indicated by the shift of the edge position and white line to lower energy, in agreement with the conventional XANES data described above. Two peaks in the pre-edge region arising from t_2g and e_g orbitals are identified as A_1 (low energy) and A_2 (high energy) (Figure 5c). Both peaks slightly shift toward lower energies, with the A_2 peak decreasing in intensity more significantly as the potential is made more negative. For $CaMnO_3$ (Figure 5b), stepping the potential to more negative values results in a more dramatic shift in the Mn edge position by ∼6 eV toward lower energy. The pre-edge region (Figure 5d) is characterized by a single more intense peak with a low-energy shoulder at 1.4 and 0.5 V, with only the A_1 peak clearly observed at 0.2 V. As in the case of the conventional XANES spectra, the complex dependency of the pre-edge features on geometry and ligand environment makes further identification of the relative fractions of the Mn species by linear combination fitting to the limited HERFD-XANES reference sample spectra collected inappropriate. However, these data do suggest a stronger potential dependence of the valency and coordination environment of Mn for $CaMnO_3$ than for $LaMnO_3$ in agreement with the conventional XAS data.

Further details of the Mn valency can be obtained by analysis of XES, taking advantage of the spin, oxidation state, and ligand sensitivity of the Mn Kβ lines.[35,36] Figure 5 compares the Mn Kβ XES of $LaMnO_3$ (a) and $CaMnO_3$ (b) as a function of the applied potential. The spectra feature a strong K$\beta_{1,3}$ peak and a broad Kβ' shoulder at lower emitted energies due to different 3d spin states.[26] Upon changing the potential from 1.4 to 0.2 V, the Mn valence decrease is reflected in the shift of the K$\beta_{1,3}$ maximum to higher energy and accompanied by intensity changes in the Kβ' region. When comparing the spectra with those collected for the reference samples (Figure S9), the *in situ* spectra collected for $LaMnO_3$ lie in between those for the Mn^{4+} and Mn^{3+} references, whereas in the case of $CaMnO_3$, the spectra lie in between those for Mn^{4+} and Mn^{2+}.

Previous XES studies have shown that such spectra can be fitted as a linear combination of the Kβ of the constituent cation species.[37−42] The normalized Mn-Kβ spectra for the reference samples (Figure S9) collected in this study were thus linearly combined to fit the Mn-Kβ spectra for $LaMnO_3$ and $CaMnO_3$. Figure 5c,d shows the normalized Mn Kβ spectra for the $LaMnO_3$ and $CaMnO_3$ electrodes at the open-circuit potential (OCP, corresponding to 1.9 V) as a combination of the

https://doi.org/10.1021/acscatal.1c00997
ACS Catal. 2021, 11, 6431−6439

reference standards (fits for the different potentials can be found in Figure S10 and Table S5, as well as statistics of the fits in Table S6). The results yield an average oxidation state of +3.4 for $LaMnO_3$ and +4.1 for $CaMnO_3$ at OCP with the relative fractions of the Mn^{2+}, Mn^{3+}, and Mn^{4+} species shown in Figure 5e,f. Application of 1.4 V results in an increase in the Mn^{4+} and decrease in the Mn^{3+} percentage for $LaMnO_3$ and a corresponding but smaller change for $CaMnO_3$. Decreasing the potential to 0.5 V and then to 0.2 V results in conversion of the Mn^{4+} ions to Mn^{3+} for $LaMnO_3$, with little change in the percentage of Mn^{2+}. In contrast, the Mn^{4+} ions are observed to be converted to both Mn^{3+} and Mn^{2+} for the $CaMnO_3$ electrode. As evidenced by the EXAFS data presented above (Figure 4), the perovskite structure is not retained at 0.2 V for $CaMnO_3$. Further evidence of this structural change was observed in the *ex situ* X-ray diffraction (XRD) obtained on the dried electrodes after the XES and HERFD-XANES measurements in Figure S11. We propose that it is this over reduction and increase in the fraction of Mn^{2+} that result in the structural changes accompanying the formation of oxygen vacancies.

The implications of the trends in Figure 5e,f are crucially important in correlating the intrinsic electrochemical responses of the perovskites and their electrocatalytic activity toward the ORR. As shown in Figure 1, the pseudo-capacitive responses in the $LaMnO_3$ voltammetric profile coincide with significant changes in XES, confirming that Mn 3d states are being populated/depopulated across the potential range in which the ORR is taking place. On the other hand, the relatively weak changes in the XES features observed in $CaMnO_3$ across the same potential range suggest that only a fraction of the large pseudocapacitive responses is linked to Mn 3d states. It is not entirely clear which orbitals contribute to the density of states responsible for the pseudo-capacitive responses in $CaMnO_3$, although electronic structure calculations by Molinari *et al.* have shown a sizeable density of O 2p states within the band gap of partially reduced $CaMnO_3$.[43]

The tolerance of the catalysts to repeated cycles 1000 times to simulate an accelerated stress test (AST) was further investigated using conventional XAS and XRD (experimental details of AST can be found in the Methods Section and cyclic voltammograms recorded before and after the AST are presented in Figure S12). Figure 6 shows the *ex situ* XANES and Fourier transforms of the EXAFS data collected before and after the AST (fits to the EXAFS data are presented in Figure S13 and fitting parameters in Table S7, with the XRD data shown in Figure S14). All data sets confirm the results from the *in situ* XAS measurements presented above, with the $LaMnO_3$ undergoing very little structural change, while the perovskite structure is significantly degraded for the $CaMnO_3$ electrocatalyst. In the case of $LaMnO_3$, it can be observed that the perovskite structure is maintained after the AST, with only a slight expansion of the Mn−La distance. In the case of $CaMnO_3$, the perovskite structure is no longer observed after the AST, and the Mn−O coordination has changed to tetrahedral (instead of an octahedral). Although the full structure is still unknown, it is highly likely that this is a mixture of different phases. Literature studies on MnO_x thin films exposed to an ORR-relevant potential of 0.7 V *versus* RHE showed the production of a disordered $Mn_3^{II,III,III}O_4$ phase.[20]

DISCUSSION

Our data show that the pseudo-capacitive responses observed in the voltammograms (Figure 1a) are associated with changes in the electron population of Mn 3d states in $LaMnO_3$ which are manifest at the ORR onset potential (Figure 1b). On the other hand, changes in the redox states of Mn sites are observed at a more negative potential in $CaMnO_3$, despite a significant pseudo-capacitive current, which is consistent with the lower activity toward the ORR. While *in situ* XANES and HERFD-XANES correspond to a greater fraction of Mn^{3+} for $LaMnO_3$ than for $CaMnO_3$ over the potential range for which ORR is observed, further details were obtained from XES (Figure 5). For $LaMnO_3$, these measurements showed that Mn^{4+} was found to persist throughout the potential range over which the RRDE measurements were conducted, wherein less of the $2e^-$ ORR product was observed at the ring than was found for $CaMnO_3$. In contrast, the XES data of $CaMnO_3$ showed that the fraction of Mn^{4+} states significantly decreases at potentials more negative than 0.6 V *versus* RHE. Furthermore, the EXAFS data show that while the Mn−O distance for $LaMnO_3$ was found to be stable (or even contracting a little) over the potential range, that for $CaMnO_3$ increased as the potential was made more negative. Such an expansion favors side-on adsorption of O_2,[17] and this agrees with the increased fraction of hydroperoxide formed compared to $LaMnO_3$.

There has been some suggestions in the literature that oxygen vacancies may participate in the ORR by turning on the bidentate adsorption of O_2,[44] stabilizing the HO_2^- species, which thus yields more of the $4e^-$ reduction products. For both $LaMnO_3$ and $CaMnO_3$ reduction of the Mn ions was found to be accompanied by the formation of oxygen vacancies as evidenced in the EXAFS, evidenced as a decrease in the Mn−O coordination number. The EXAFS results shown in our study suggest that $LaMnO_3$ is better able to tolerate the formation of these vacancies. In contrast, the EXAFS data suggest that $CaMnO_3$ is not able to tolerate the formation of oxygen vacancies with the perovskite structure being lost, presumably due to the formation of Mn^{2+} ions and correspondingly greater oxygen loss, which then contributes to the structural collapse of $CaMnO_3$ observed following accelerated stress testing.

The results presented above demonstrate the added information that may be obtained from a combined approach of *ex situ* and *in situ* X-ray characterization of such electrocatalysts and, in particular, the use of XES to provide details of the relative populations of the various oxidation states, compared to the average oxidation state provided by XANES measurements. The combined use of these techniques has enabled a deeper understanding of the processes observed as the pseudocapacitive response in the voltammetry of these Mn oxides and highlighted the importance of the $Mn^{4+/3+}$redox couple in achieving the full $4e^-$ reduction of oxygen.

METHODS SECTION

Sample Preparation. $(La,Ca)MnO_3$ perovskite nanoparticles were synthesized employing an ionic liquid-based route described in previous works.[13,14,29] First, a dispersion of $Mn(NO_3)_3$ (0.5 mL, 0.1 M in H_2O) and 0.5 mL of the corresponding A-site metal nitrate (0.5 mL, 0.1 M in H_2O) in 1-ethyl-3-methylimidazolium acetate (1 mL) was prepared and kept under stirring conditions. After heating at 80 °C for 4 h to ensure all water was removed, cellulose (100 mg) was added and the mixture was stirred for 20 min. The gel-like mixture was calcined for 2 h at 700 °C for $LaMnO_3$ and 850 °C for $CaMnO_3$, to ensure single-phase formation.

Material Characterization. XRD patterns were recorded using a Bruker AXS D8 Advance diffractometer with a $\theta-\theta$

https://doi.org/10.1021/acscatal.1c00997
ACS Catal. 2021, 11, 6431−6439

configuration, using Cu Kα radiation (λ = 0.154 nm). The XRD patterns were refined by the Rietveld method using the FULLPROF program.[45,46] The following parameters were refined: scale factor, background coefficients, zero-point error, and positional coordinates. The isotropic thermal factors for all the atoms were fixed to a standard value of 1 Å^2. No cation deficiency was detected, and so, the occupancy factors for both $LaMnO_3$ and $CaMnO_3$ were fixed to 1. XRD patterns of the as-synthetised $LaMnO_3$ and $CaMnO_3$ oxide nanoparticles can be found in Figure S15 and structural parameters obtained by Rietveld method in Table S8. Transmission electron microscopy (TEM) was performed using a JEOL JEM-1400Plus and representative images for both materials are shown in Figure S16.

Rotating Ring-Disk Electrochemical Measurements. A three-electrode cell was used to conduct the electrochemistry experiments, using a rotating ring-disk electrode (RRDE) fitted to an ALS rotation controller and connected to a CompactStat bipotentiostat (Ivium). The RRDE electrode consisted of a 4 mm glassy carbon disk surrounded by a Pt ring. The collection efficiency was experimentally determined to be 0.4. A graphite rod and a Hg/HgO (in 0.1 M NaOH) were used as counter and reference electrodes, respectively. Measurements were recorded in 0.1 M KOH solution saturated with either purified Ar or O_2. The sample loading (per unit area of the glassy carbon disk) on the electrode surface was 250 μg_{OXIDE} cm^{-2}, 50 μg_{VULCAN} cm^{-2}, and 50 μg_{NAFION} cm^{-2}.

Preparation of Electrodes and *In Situ* XAS and XES Measurements. Button electrodes were prepared by painting the catalyst ink onto a carbon paper support with a loading of 0.5 mg Mn cm^{-2}. All measurements were collected *in situ*, using our custom-designed electrochemical cells[47] connected to an Autolab PGSTAT101 potentiostat. Measurements were collected in the N_2-purged 0.1 M KOH electrolyte.

EXAFS measurements were carried out at room temperature at the SAMBA beamline of Soleil Synchrotron (Saclay, France).[48] The beamline is equipped with a sagittally focusing Si 220 monochromator and two Pd-coated collimating/focusing mirrors to remove higher harmonics. Calibration of the monochromator was carried out using Mn foil, and XAFS spectra were recorded in the fluorescence mode at the Mn K-edge (6539 eV) using a Canberra 35-elements monolithic planar Ge pixel array detector. The spectra were aligned using the Mn foil response. The data were analyzed using the Athena and Artemis softwares.[49]

XES and HERFD-XANES measurements were conducted at Beamline I20-Scanning, of Diamond Light Source,[50,51] operating with a ring energy of 3 GeV and at a current of 300 mA. The beamline is equipped with an in-house-designed four-bounce scanning Si(111) monochromator, and the harmonic rejection was achieved using two Si-coated mirrors. An X-ray emission spectrometer based on a 1 m diameter Rowland circle operating in the Johann configuration in the vertical plane with three spherically bent Ge(440) analyzers to collect the emission signal was used for the experiment (see Figure S17).[52] The XES spectra have been normalized with respect to their total area using the range 6465−6497 eV. All the HERFD-XANES measurements were collected at the peak of K$\beta_{1,3}$ line, and nonresonant XES spectra were measured 100 eV above the absorption edge of Mn.

AST Cycling. Studies on the stability of the proposed materials was carried out by performing accelerated stress tests, where the potential was cycled between 1.1 and 0.6 V *versus* RHE at 0.050 V s^{-1}, during 1000 cycles, following the DOE standard procedures.

■ ASSOCIATED CONTENT

Supporting Information

The Supporting Information is available free of charge at https://pubs.acs.org/doi/10.1021/acscatal.1c00997.

Percentage of peroxide formation during the ORR; Mn XANES of references; calibration plot for the determination of the average Mn oxidation state from the edge positions; Mn K-edge XANES and k^3-weighted χ and k^3-weighted Fourier transform EXAFS data and fits for the pellets; k^3-weighted χ data and k^3-weighted Fourier transform EXAFS data and fits for the dry electrodes; k^3-weighted χ data and k^3-weighted Fourier transform EXAFS data and fits for the data collected at 1.4 V;k^3-weighted χ and k^3-weighted Fourier transform EXAFS data and first shell fits for the data collected at different potentials; HERFD-XANES spectra at the K$\beta_{1,3}$ line of the reference compounds; Mn Kβ XES spectra of references; linear combination fits of the Mn Kβ XES spectra of the data collected at different potentials; *ex situ* X-ray powder diffraction measured before and after electrochemistry; cyclic voltammograms of the $LaMnO_3$ and $CaMnO_3$ electrodes before and after the AST; k^3-weighted χ data and k^3-weighted Fourier transform EXAFS data and fits for the data collected after AST; *ex situ* X-ray powder diffraction measured before and after AST; XRD patterns of the as-synthesized oxides; representative TEM of synthesized oxide nanoparticles; and schematic view of the I20-scanning branch of the Diamond Light Source (PDF)

■ AUTHOR INFORMATION

Corresponding Authors

Veronica Celorrio − *Diamond Light Source Ltd, Didcot OX11 0DE, U.K.*; orcid.org/0000-0002-2818-3844; Email: Veronica.Celorrio@diamond.ac.uk

David J. Fermin − *School of Chemistry, University of Bristol, Bristol BS8 1TS, U.K.*; orcid.org/0000-0002-0376-5506; Email: David.Fermin@bristol.ac.uk

Andrea E. Russell − *School of Chemistry, University of Southampton, Southampton SO17 1BJ, U.K.*; orcid.org/0000-0002-8382-6443; Email: a.e.russell@soton.ac.uk

Authors

Andrew S. Leach − *School of Chemistry, University of Southampton, Southampton SO17 1BJ, U.K.*

Haoliang Huang − *School of Chemistry, University of Southampton, Southampton SO17 1BJ, U.K.*

Shusaku Hayama − *Diamond Light Source Ltd, Didcot OX11 0DE, U.K.*

Adam Freeman − *Diamond Light Source Ltd, Didcot OX11 0DE, U.K.*

David W. Inwood − *School of Chemistry, University of Southampton, Southampton SO17 1BJ, U.K.*

Complete contact information is available at: https://pubs.acs.org/10.1021/acscatal.1c00997

Author Contributions

V.C. and A.E.R. conceived the experiments. V.C. synthesized the materials and performed the electrochemistry experiments. V.C.

https://doi.org/10.1021/acscatal.1c00997
ACS Catal. 2021, 11, 6431−6439

and D.J.F. analyzed the electrochemical data. EXAFS data were collected by V.C., A.S.L., and D.I. XES and HERFD-XANES data were collected by S.H., A.F., V.C., A.S.L., H.H., and A.E.R. EXAFS, XES, and HERFD-XANES data analyses were performed by V.C. and A.E.R. All authors contributed to the analysis of the results, discussion, and writing and revision of the manuscript. All authors have given approval to the final version of the manuscript.

Notes

The authors declare no competing financial interest.

Data are available at the University of Southampton data repository, https://doi.org/10.5258/SOTON/D1810.

■ ACKNOWLEDGMENTS

V.C., A.E.R., and D.J.F. kindly thank the UK Catalysis Hub for resources and support provided *via* the membership of the UK Catalysis Hub Consortium (EPSRC grants EP/K014706/1 and EP/K014714/1). The authors wish to acknowledge the Diamond Light Source for provision of beamtime (SP16479). EXAFS experiments were performed on the SAMBA beamline at SOLEIL Synchrotron, France (proposal number 20160321). We are grateful to Dr Andrea Zitolo for assistance and to the SOLEIL staff for smoothly running the facility. V.C. is in debt to the STFC Batteries Network (ST/N002385/1) for the support through the STFC Batteries Early Career Award. H.H. acknowledges the China Scholarship Council (201608440295) and the University of Southampton and A.S.L. acknowledges City Technology and the EPSRC CASE award scheme and D.I. Johnson Matthey and the EPSRC CASE award scheme for support of their Ph.D. studentships.

■ REFERENCES

(1) Ge, X.; Sumboja, A.; Wuu, D.; An, T.; Li, B.; Goh, F. W. T.; Hor, T. S. A.; Zong, Y.; Liu, Z. Oxygen Reduction in Alkaline Media: From Mechanisms to Recent Advances of Catalysts. *ACS Catal.* **2015**, *5*, 4643−4667.

(2) Rana, M.; Mondal, S.; Sahoo, L.; Chatterjee, K.; Karthik, P. E.; Gautam, U. K. Emerging Materials in Heterogeneous Electrocatalysis Involving Oxygen for Energy Harvesting. *ACS Appl. Mater. Interfaces* **2018**, *10*, 33737−33767.

(3) Wu, J.; Yang, H. Platinum-Based Oxygen Reduction Electrocatalysts. *Acc. Chem. Res.* **2013**, *46*, 1848−1857.

(4) Fabbri, E.; Habereder, A.; Waltar, K.; Kötz, R.; Schmidt, T. J. Developments and perspectives of oxide-based catalysts for the oxygen evolution reaction. *Catal. Sci. Technol.* **2014**, *4*, 3800−3821.

(5) Chen, D.; Chen, C.; Baiyee, Z. M.; Shao, Z.; Ciucci, F. Nonstoichiometric Oxides as Low-Cost and Highly-Efficient Oxygen Reduction/Evolution Catalysts for Low-Temperature Electrochemical Devices. *Chem. Rev.* **2015**, *115*, 9869−9921.

(6) Gu, X.-K.; Samira, S.; Nikolla, E. Oxygen Sponges for Electrocatalysis: Oxygen Reduction/Evolution on Nonstoichiometric, Mixed Metal Oxides. *Chem. Mater.* **2018**, *30*, 2860−2872.

(7) Xiong, Y.; Yang, Y.; Feng, X.; DiSalvo, F. J.; Abruña, H. D. A Strategy for Increasing the Efficiency of the Oxygen Reduction Reaction in Mn-Doped Cobalt Ferrites. *J. Am. Chem. Soc.* **2019**, *141*, 4412−4421.

(8) Zhao, Q.; Yan, Z.; Chen, C.; Chen, J. Spinels: Controlled Preparation, Oxygen Reduction/Evolution Reaction Application, and Beyond. *Chem. Rev.* **2017**, *117*, 10121−10211.

(9) Bonnefont, A.; Ryabova, A. S.; Schott, T.; Kéranguéven, G.; Istomin, S. Y.; Antipov, E. V.; Savinova, E. R. Challenges in the understanding oxygen reduction electrocatalysis on transition metal oxides. *Curr. Opin. Electrochem.* **2019**, *14*, 23−31.

(10) Stoerzinger, K. A.; Risch, M.; Han, B.; Shao-Horn, Y. Recent Insights into Manganese Oxides in Catalyzing Oxygen Reduction Kinetics. *ACS Catal.* **2015**, *5*, 6021−6031.

(11) Bockris, J. O. M.; Otagawa, T. The Electrocatalysis of Oxygen Evolution on Perovskites. *J. Electrochem. Soc.* **1984**, *131*, 290−302.

(12) Suntivich, J.; Gasteiger, H. A.; Yabuuchi, N.; Nakanishi, H.; Goodenough, J. B.; Shao-Horn, Y. Erratum: Design principles for oxygen-reduction activity on perovskite oxide catalysts for fuel cells and metal-air batteries. *Nat. Chem.* **2011**, *3*, 647.

(13) Celorrio, V.; Calvillo, L.; Granozzi, G.; Russell, A. E.; Fermin, D. J. AMnO3 (A = Sr, La, Ca, Y) Perovskite Oxides as Oxygen Reduction Electrocatalysts. *Top. Catal.* **2018**, *61*, 154−161.

(14) Celorrio, V.; Calvillo, L.; Dann, E.; Granozzi, G.; Aguadero, A.; Kramer, D.; Russell, A. E.; Fermín, D. J. Oxygen reduction reaction at LaxCa1−xMnO3 nanostructures: interplay between A-site segregation and B-site valency. *Catal. Sci. Technol.* **2016**, *6*, 7231−7238.

(15) Stoerzinger, K. A.; Lü, W.; Li, C.; Ariando; Venkatesan, T.; Shao-Horn, Y. Highly Active Epitaxial La(1-x)SrxMnO3 Surfaces for the Oxygen Reduction Reaction: Role of Charge Transfer. *J. Phys. Chem. Lett.* **2015**, *6*, 1435−1440.

(16) Stoerzinger, K. A.; Risch, M.; Suntivich, J.; Lü, W. M.; Zhou, J.; Biegalski, M. D.; Christen, H. M.; Ariando; Venkatesan, T.; Shao-Horn, Y. Oxygen electrocatalysis on (001)-oriented manganese perovskite films: Mn valency and charge transfer at the nanoscale. *Energy Environ. Sci.* **2013**, *6*, 1582−1588.

(17) Du, J.; Zhang, T.; Cheng, F.; Chu, W.; Wu, Z.; Chen, J. Nonstoichiometric Perovskite CaMnO3−δ for Oxygen Electrocatalysis with High Activity. *Inorg. Chem.* **2014**, *53*, 9106−9114.

(18) Kan, D.; Orikasa, Y.; Nitta, K.; Tanida, H.; Kurosaki, R.; Nishimura, T.; Sasaki, T.; Guo, H.; Ozaki, Y.; Uchimoto, Y.; Shimakawa, Y. Overpotential-Induced Introduction of Oxygen Vacancy in La0.67Sr0.33MnO3 Surface and Its Impact on Oxygen Reduction Reaction Catalytic Activity in Alkaline Solution. *J. Phys. Chem. C* **2016**, *120*, 6006−6010.

(19) Ryabova, A. S.; Napolskiy, F. S.; Poux, T.; Istomin, S. Y.; Bonnefont, A.; Antipin, D. M.; Baranchikov, A. Y.; Levin, E. E.; Abakumov, A. M.; Kéranguéven, G.; Antipov, E. V.; Tsirlina, G. A.; Savinova, E. R. Rationalizing the Influence of the Mn(IV)/Mn(III) Red-Ox Transition on the Electrocatalytic Activity of Manganese Oxides in the Oxygen Reduction Reaction. *Electrochim. Acta* **2016**, *187*, 161−172.

(20) Gorlin, Y.; Lassalle-Kaiser, B.; Benck, J. D.; Gul, S.; Webb, S. M.; Yachandra, V. K.; Yano, J.; Jaramillo, T. F. In Situ X-ray Absorption Spectroscopy Investigation of a Bifunctional Manganese Oxide Catalyst with High Activity for Electrochemical Water Oxidation and Oxygen Reduction. *J. Am. Chem. Soc.* **2013**, *135*, 8525−8534.

(21) Risch, M.; Stoerzinger, K. A.; Han, B.; Regier, T. Z.; Peak, D.; Sayed, S. Y.; Wei, C.; Xu, Z.; Shao-Horn, Y. Redox Processes of Manganese Oxide in Catalyzing Oxygen Evolution and Reduction: An in Situ Soft X-ray Absorption Spectroscopy Study. *J. Phys. Chem. C* **2017**, *121*, 17682−17692.

(22) Lima, F. H. B.; Calegaro, M. L.; Ticianelli, E. A. Electrocatalytic activity of manganese oxides prepared by thermal decomposition for oxygen reduction. *Electrochim. Acta* **2007**, *52*, 3732−3738.

(23) Safonova, O. V.; Tromp, M.; van Bokhoven, J. A.; de Groot, F. M. F.; Evans, J.; Glatzel, P. Identification of CO Adsorption Sites in Supported Pt Catalysts Using High-Energy-Resolution Fluorescence Detection X-ray Spectroscopy. *J. Phys. Chem. B* **2006**, *110*, 16162−16164.

(24) Eisenberger, P.; Platzman, P. M.; Winick, H. X-Ray Resonant Raman Scattering: Observation of Characteristic Radiation Narrower than the Lifetime Width. *Phys. Rev. Lett.* **1976**, *36*, 623−626.

(25) Glatzel, P.; Sikora, M.; Smolentsev, G.; Fernández-García, M. Hard X-ray photon-in photon-out spectroscopy. *Catal. Today* **2009**, *145*, 294−299.

(26) Vankó, G.; Neisius, T.; Molnár, G.; Renz, F.; Kárpáti, S.; Shukla, A.; de Groot, F. M. F. Probing the 3d Spin Momentum with X-ray Emission Spectroscopy: The Case of Molecular-Spin Transitions. *J. Phys. Chem. B* **2006**, *110*, 11647−11653.

(27) Traulsen, M. L.; de Carvalho, H. W. P.; Zielke, P.; Grunwaldt, J.-D. The Effect of Electrical Polarization on Electronic Structure in LSM Electrodes: An Operando XAS, RIXS and XES Study. *J. Electrochem. Soc.* **2017**, *164*, F3064−F3072.
(28) Hardin, W. G.; Mefford, J. T.; Slanac, D. A.; Patel, B. B.; Wang, X.; Dai, S.; Zhao, X.; Ruoff, R. S.; Johnston, K. P.; Stevenson, K. J. Tuning the Electrocatalytic Activity of Perovskites through Active Site Variation and Support Interactions. *Chem. Mater.* **2014**, *26*, 3368−3376.
(29) Celorrio, V.; Dann, E.; Calvillo, L.; Morgan, D. J.; Hall, S. R.; Fermin, D. J. Oxygen Reduction at Carbon-Supported Lanthanides: The Role of the B-Site. *ChemElectroChem* **2016**, *3*, 283−291.
(30) Su, H.-Y.; Gorlin, Y.; Man, I. C.; Calle-Vallejo, F.; Nørskov, J. K.; Jaramillo, T. F.; Rossmeisl, J. Identifying active surface phases for metal oxide electrocatalysts: a study of manganese oxide bi-functional catalysts for oxygen reduction and water oxidation catalysis. *Phys. Chem. Chem. Phys.* **2012**, *14*, 14010−14022.
(31) Wiechen, M.; Berends, H.-M.; Kurz, P. Wateroxidation catalysed by manganese compounds: from complexes to "biomimetic rocks". *Dalton Trans.* **2012**, *41*, 21−31.
(32) Ignatov, A. Y.; Khalid, S.; Sujoy, R.; Ali, N. Theoretical study of MnK-edge in La1-xCaxMnO3. *J. Synchrotron Radiat.* **2001**, *8*, 898−900.
(33) Chaboy, J. Relationship between the structural distortion and the Mn electronic state in La1−xCaxMnO3: a MnK-edge XANES study. *J. Synchrotron Radiat.* **2009**, *16*, 533−544.
(34) Croft, M.; Sills, D.; Greenblatt, M.; Lee, C.; Cheong, S.-W.; Ramanujachary, K. V.; Tran, D. Systematic Mn d-configuration change in theLa1−xCaxMnO3system: A Mn K-edge XAS study. *Phys. Rev. B: Condens. Matter Mater. Phys.* **1997**, *55*, 8726−8732.
(35) Lafuerza, S.; García, J.; Subías, G.; Blasco, J.; Glatzel, P. High-resolution Mn K-edge x-ray emission and absorption spectroscopy study of the electronic and local structure of the three different phases in $Nd_{0.5}Sr_{0.5}MnO_3$. *Phys. Rev. B* **2016**, *93*, 205108.
(36) Tyson, T. A.; Qian, Q.; Kao, C.-C.; Rueff, J.-P.; de Groot, F. M. F.; Croft, M.; Cheong, S.-W.; Greenblatt, M.; Subramanian, M. A. Valence state of Mn in Ca-dopedLaMnO3studied by high-resolutionMnKβemission spectroscopy. *Phys. Rev. B: Condens. Matter Mater. Phys.* **1999**, *60*, 4665−4674.
(37) Bordage, A.; Trannoy, V.; Proux, O.; Vitoux, H.; Moulin, R.; Bleuzen, A. In situ site-selective transition metal K-edge XAS: a powerful probe of the transformation of mixed-valence compounds. *Phys. Chem. Chem. Phys.* **2015**, *17*, 17260−17265.
(38) Bhargava, A.; Chen, C. Y.; Finkelstein, K. D.; Ward, M. J.; Robinson, R. D. X-ray emission spectroscopy: an effective route to extract site occupation of cations. *Phys. Chem. Chem. Phys.* **2018**, *20*, 28990−29000.
(39) Kühn, T.-J.; Hormes, J.; Matoussevitch, N.; Bönnemann, H.; Glatzel, P. Site-Selective High-Resolution X-ray Absorption Spectroscopy and High-Resolution X-ray Emission Spectroscopy of Cobalt Nanoparticles. *Inorg. Chem.* **2014**, *53*, 8367−8375.
(40) Peng, G.; deGroot, F. M. F.; Haemaelaeinen, K.; Moore, J. A.; Wang, X.; Grush, M. M.; Hastings, J. B.; Siddons, D. P.; Armstrong, W. H. High-resolution manganese x-ray fluorescence spectroscopy. Oxidation-state and spin-state sensitivity. *J. Am. Chem. Soc.* **1994**, *116*, 2914−2920.
(41) Glatzel, P.; Jacquamet, L.; Bergmann, U.; de Groot, F. M. F.; Cramer, S. P. Site-Selective EXAFS in Mixed-Valence Compounds Using High-Resolution Fluorescence Detection: A Study of Iron in Prussian Blue. *Inorg. Chem.* **2002**, *41*, 3121−3127.
(42) Celorrio, V.; Tiwari, D.; Calvillo, L.; Leach, A.; Huang, H.; Granozzi, G.; Alonso, J. A.; Aguadero, A.; Pinacca, R. M.; Russell, A. E.; Fermin, D. J. Electrocatalytic Site Activity Enhancement via Orbital Overlap in A2MnRuO7 (A = Dy3+, Ho3+, and Er3+) Pyrochlore Nanostructures. *ACS Appl. Energy Mater.* **2021**, *4*, 176−185.
(43) Molinari, M.; Tompsett, D. A.; Parker, S. C.; Azough, F.; Freer, R. Structural, electronic and thermoelectric behaviour of CaMnO3 and CaMnO(3−δ). *J. Mater. Chem. A* **2014**, *2*, 14109−14117.
(44) Matsumoto, Y.; Yoneyama, H.; Tamura, H. The Mechanism of Oxygen Reduction at a LaNiO3Electrode. *Bull. Chem. Soc. Jpn.* **1978**, *51*, 1927−1930.
(45) Rietveld, H. M. A profile refinement method for nuclear and magnetic structures. *J. Appl. Crystallogr.* **1969**, *2*, 65−71.
(46) Rodríguez-Carvajal, J. Recent advances in magnetic structure determination by neutron powder diffraction. *Phys. B* **1993**, *192*, 55−69.
(47) Sardar, K.; Petrucco, E.; Hiley, C. I.; Sharman, J. D. B.; Wells, P. P.; Russell, A. E.; Kashtiban, R. J.; Sloan, J.; Walton, R. I. Water-Splitting Electrocatalysis in Acid Conditions Using Ruthenate-Iridate Pyrochlores. *Angew. Chem.* **2014**, *126*, 11140−11144.
(48) Belin, S.; Briois, V.; Traverse, A.; Idir, M.; Moreno, T.; Ribbens, M. SAMBA a New Beamline at SOLEIL for XRay Absorption Spectroscopy in the 440keV Energy Range. *Phys. Scr.* **2005**, *T115*, 980−983.
(49) Ravel, B.; Newville, M. ATHENA,ARTEMIS,HEPHAESTUS: data analysis for X-ray absorption spectroscopy usingIFEFFIT. *J. Synchrotron Radiat.* **2005**, *12*, 537−541.
(50) Diaz-Moreno, S.; Amboage, M.; Basham, M.; Boada, R.; Bricknell, N. E.; Cibin, G.; Cobb, T. M.; Filik, J.; Freeman, A.; Geraki, K.; Gianolio, D.; Hayama, S.; Ignatyev, K.; Keenan, L.; Mikulska, I.; Mosselmans, J. F. W.; Mudd, J. J.; Parry, S. A. The Spectroscopy Village at Diamond Light Source. *J. Synchrotron Radiat.* **2018**, *25*, 998−1009.
(51) Hayama, S.; Duller, G.; Sutter, J. P.; Amboage, M.; Boada, R.; Freeman, A.; Keenan, L.; Nutter, B.; Cahill, L.; Leicester, P.; Kemp, B.; Rubies, N.; Diaz-Moreno, S. The scanning four-bounce monochromator for beamline I20 at the Diamond Light Source. *J. Synchrotron Radiat.* **2018**, *25*, 1556−1564.
(52) Johann, H. H. Die Erzeugung lichtstarker Röntgenspektren mit Hilfe von Konkavkristallen. *Z. Phys.* **1931**, *69*, 185−206.

https://doi.org/10.1021/acscatal.1c00997
ACS Catal. 2021, 11, 6431−6439